Materials Advances

ROYAL SOCIETY OF CHEMISTRY

PAPER

View Article Online
View Journal | View Issue

Cite this: *Mater. Adv.*, 2023, 4, 5238

The impact of Ni and Zn doping on the thermal durability and thermoelectric variables of pristine CuSe nanoparticles†

Sefali R. Patel, *[a] Sunil H. Chaki, *[ab] Mitesh B. Solanki,[c] Rohitkumar M. Kannaujiya,[a] Zubin R. Parekh,[a] Ankurkumar J. Khimani[d] and Milind P. Deshpande[a]

Copper selenide nanomaterials are recognized to possess thermoelectric characteristics, becoming a strong contender to unite materials science and energy technology with effective use in practical applications in extreme environments. Nanoparticles of pure CuSe, as well as Ni- and Zn-doped CuSe, are synthesized *via* an elementary co-precipitation strategy, with their structural and compositional verification achieved through preliminary characterization. In this endeavor, the authors embark on a first-of-its-kind investigation of the thermal attributes of as-synthesized Ni and Zn-doped CuSe nanoparticles. The thermogravimetric profiles for pristine, Ni- and Zn-doped CuSe nanoparticles are acquired under neutral nitrogen (N_2) conditions spanning ambient temperature to 793 K. The assessment demonstrated that all nanoparticles tested went through a two-step breakdown, showcasing a maximum weight reduction of 26.08% for pristine CuSe and the lowest weight decrement of 16.87% for Zn-doped CuSe nanoparticles. The experimental assessment of thermal stability is substantiated through a comprehensive theoretical analysis of phonon dynamic stability that provides profound insight into the thermal characteristics of the as-synthesized nanoparticles. Density functional theory is employed to scrutinize the phonon dynamic stability within CuSe with Ni and Zn as dopants. The Kissinger framework is employed to estimate the thermodynamic coefficients conveying the non-spontaneous disintegration of all nanoparticles. All five samples are proven to be semiconductors based on the variations in Seebeck coefficient (S), dc electrical conductivity (σ), and thermal conductivity (κ) from ambient temperature to 523 K. The investigation of temperature-induced variations in the power factor ($S^2\sigma$) and figure of merit (ZT) elucidated that Ni- and Zn-doped nanoparticles exhibit superior values in comparison to pure CuSe nanoparticles. The optimum ZT metric of 1.28 is attained for 10% Zn-doped CuSe nanoparticles at 523 K. A detailed discussion of the findings is provided.

Received 23rd July 2023,
Accepted 15th September 2023

DOI: 10.1039/d3ma00454f

rsc.li/materials-advances

1. Introduction

Transition metal chalcogenide (TMC) nanomaterials possess a range of remarkable properties that make TMCs highly versatile for applications in electronics, energy conversion, catalysis, sensors, and many more.[1–7] Continued research and development in this field has the potential to revolutionize various industries and contribute to technological advancements in the coming years. The importance of copper selenides within the TMC family lies in their diverse range of applications, including thermoelectric devices, photovoltaics, energy storage, catalysis, and optoelectronics.[8–10] Copper selenides comprise a varied subgroup of p-type semiconductors that exist in a wide variety of stoichiometric phases, such as CuSe,[11] Cu_2Se, $CuSe_2$,[12] Cu_3Se_2,[13] Cu_5Se_4,[14] and Cu_7Se_4,[15] as well as non-stoichiometric forms of $Cu_{2-x}Se$ $(2.00 \geq 2 - x \geq 1.72)$.[16]

The importance of single-phase CuSe nanoparticles lies in their unique properties and potential applications, such as optoelectronic devices, energy harvesting and waste heat recovery, catalysis, photothermal therapy, *etc.*[9,17,18] Metal doping in binary CuSe semiconductors plays a crucial role in enhancing

[a] *P. G. Department of Physics, Sardar Patel University, Vallabh Vidyanagar – 388120, Gujarat, India. E-mail: sefalipatel12345@gmail.com, sunilchaki@yahoo.co.in*
[b] *Department of Applied & Interdisciplinary Sciences, IICISST, Sardar Patel University, Vallabh Vidyanagar – 388120, Gujarat, India*
[c] *Department of Physics, Parul Institute of Applied Sciences, Parul University, Waghodia, Vadodara, Gujarat, 391760, India*
[d] *Department of Physics, Shri A. N. Patel P. G. Institute of Science and Research, Anand – 388001, Gujarat, India*

† Electronic supplementary information (ESI) available. See DOI: https://doi.org/10.1039/d3ma00454f

their properties, such as ability to tune bandgap, control carrier concentration, enhance electrical conductivity, tailor optical properties, and improve stability.[19–23] These capabilities expand the range of potential applications of CuSe nanoparticles and pave the way for the development of advanced electronic, optoelectronic, and energy-related devices. Within the realm of existing literature, numerous investigations delved into transition metal-doped CuSe materials in both nanocrystal and thin film formats.[24–26] However, no scholarly discourse has reported the exploration of 5% and 10% doping levels for Ni and Zn in CuSe nanoparticles. As a consequence, the authors intended to synthesize and examine Ni and Zn-doped CuSe nanoparticles.

Over the years, copper selenide materials have garnered significant interest for their remarkable thermoelectric characteristics. Analyzing the prospective utility of the as-synthesized nanoparticles as thermoelectric materials necessitates an examination of their thermal stability, which is important to underpin consistent and efficient performance for the device. The thermogravimetric and differential thermogravimetric profiles for pure CuSe nanoparticles have been described by Josephine Ying Chyi Liew *et al.*[27] and Ibrahim Garba Shitu *et al.*[28] Also, Huan Luo *et al.* conducted a thorough thermal study with kinetic parameters for a pure CuSe compound.[29] But as far as the present researchers are cognizant, neither any thorough thermal study of 5% and 10% Ni-doped CuSe nanoparticles nor that of 5% and 10% Zn-doped CuSe nanoparticles has previously been described. Because of this, the authors investigated the thermal properties of pristine CuSe along with Ni and Zn-doped CuSe nanoparticles in this manuscript. Besides experimental thermal investigations, there is currently limited *in silico* understanding of the theoretical thermal stability within the copper selenide family. The prior research article reports the density functional theory (DFT) investigations to study the metallic behavior of hexagonal CuSe.[30] Yubo Zang *et al.* and Mikael Råsander *et al.* have employed DFT to examine the electronic structure of fluorites Cu_2X (X = S, Se, Te).[31,32] Besides these limited findings, there are neither published theoretical studies on the structural phonon dynamic stability of hexagonal klockmannite CuSe nor any for Ni- and Zn-doped CuSe. For this reason, a DFT investigation is executed on the theoretical sub-stoichiometric doping of Ni and Zn within the hexagonal crystal system of CuSe. This manuscript delves deeper into the structural relaxation and phonon dynamic stability of the CuSe hexagonal crystal system, exploring their sensitivity to the metallic impurities of Ni and Zn.

Throughout the preceding decades, thermoelectric materials captured increasing attention, attributable to their potentiality in converting industrial waste heat into electrical energy.[33–35] This quantification is typically ascertained through the material's figure of merit, denoted as *ZT*. To date, numerous scholarly works have examined the transport characteristics of Cu_2Se and $Cu_{2-x}Se$, positioning them as prospective contenders in the domain of thermoelectric materials.[36–39] However, the CuSe phase has garnered notably less attention, prompting the authors to embark on an investigation aimed at enhancing its thermoelectric properties, thereby unlocking its substantial potential across a broad spectrum of disciplines. To the best of the authors' knowledge, the first investigation of the figure of merit (*ZT*) for CuSe nanoparticles was carried out by Longbin Li *et al.*, yielding values spanning from 0.004 to 0.021.[40] Based on the authors' comprehensive literature review, no previous records documented the in-depth thermoelectric examination of CuSe nanoparticles doped with 5% and 10% Ni, as well as 5% and 10% Zn. Henceforth, within this manuscript, the authors undertook an intricate exploration concerning the thermoelectric performance of CuSe nanoparticles, modified by the incorporation of Ni and Zn dopants. This research work aims to learn about the thermoelectric impact mechanism of Ni and Zn doping on pristine CuSe nanoparticles.

2. Experimental details

In the present work, the thermal behavior of previously synthesized nanoparticles of CuSe, 5% Ni-doped CuSe, 10% Ni-doped CuSe, 5% Zn-doped CuSe, and 10% Zn-doped CuSe is investigated. In order to keep everything simple, pure CuSe is denoted by S1, 5% Ni-doped CuSe by S2, 10% Ni-doped CuSe by S3, 5% Zn-doped CuSe by S4, and 10% Zn-doped CuSe by S5. The synthesis of nanoparticles through the co-precipitation approach and their preliminary characterization are already described in the latest publication of the authors.[41] The XRD profiles of the quintet of the as-synthesized nanoparticles are elucidated in Fig. S1 (ESI†). The plotted data validated the hexagonal crystalline arrangement in all specimens, evincing structural dimensions that closely aligned with the standard data from JCPDS Card no. 034-171. Table S1 (ESI†) demonstrates the structural data derived from the XRD analysis. The in-depth structural examination of XRD profiles is elaborated on in the same recent publication by the authors.[41] The ascertained findings elucidated that crystallinity of the nanoparticles is compromised upon the substitution of host lattice ions with dopants. The EDAX assessment, portrayed in Fig. S2 (ESI†), substantiated the chemical stoichiometry of all five as-synthesized nanoparticles. The spectra unveiled solely the characteristic peaks of the individual elements, underscoring the purity of the as-synthesized samples, devoid of any extraneous impurities. The authors' publication corroborates the nanoparticles' stoichiometry *via* a juxtaposition of ascertained and standard weight proportions of Cu, Se, and the corresponding dopants Ni and Zn employing EDAX data.[41] The homogeneous dispersion of elemental constituents is affirmed through the elemental mapping micrographs for all nanoparticles, as depicted in Fig. S3 (ESI†). The FESEM micrographs presented in Fig. S4 (ESI†) revealed a spherical morphology with uniform distribution for all as-synthesized nanoparticles. All nanoparticles are investigated by X-ray photoelectron spectroscopy (XPS) using a Scienta ESCA equipped with Omicron Nano Technology. The thermogravimetric (TG), differential thermogravimetric (DTG), and differential thermal analysis (DTA) curves of all as-synthesized nanoparticles are measured using the Seiko SII-EXSTAR TG/DTA-7200 thermal analyzer. The alteration in thermoelectric

power (S) and dc electrical conductivity (σ) and variation in thermal conductivity as a consequence of temperature are examined using equipment fabricated by Supernova Technology, Vithal Udyognagar, Gujarat, India.

3. X-Ray photoelectron spectroscopy

Each nanoparticle's chemical constituents and valence level are determined through inspection of their XPS profiles shown in Fig. 1. According to the survey spectral data, all the nanoparticles comprise of elements Cu, Se, O, and C. Furthermore, the survey patterns for Ni- and Zn-doped nanoparticles demonstrate the involvement of Ni and Zn components, respectively. The weak O 1s peak around 531.2 eV and the C 1s peak at 284.8 eV are primarily attributed to the oxygen and carbon dioxide absorbed on the sample surface.[42]

The individual Cu 2p, Se 3d, Ni 2p, and Zn 2p XPS spectra are displayed in Fig. 1. As depicted in Fig. 1, the Cu 2p level appears with two prominent photoelectron peaks with binding energies of around 932.4 eV for Cu $2p_{3/2}$ and 952.2 eV for Cu $2p_{1/2}$ that correspond with the Cu^{2+} state across all five samples.[42,43] The XPS profiles of Se 2d for all samples exhibit two photoelectron bands with binding energy values of 54.2 eV and 55.0 eV, designated as Se $2d_{5/2}$ and Se $2d_{3/2}$, respectively, known as standard peaks of Se.[2–42,44] The identical patterns of

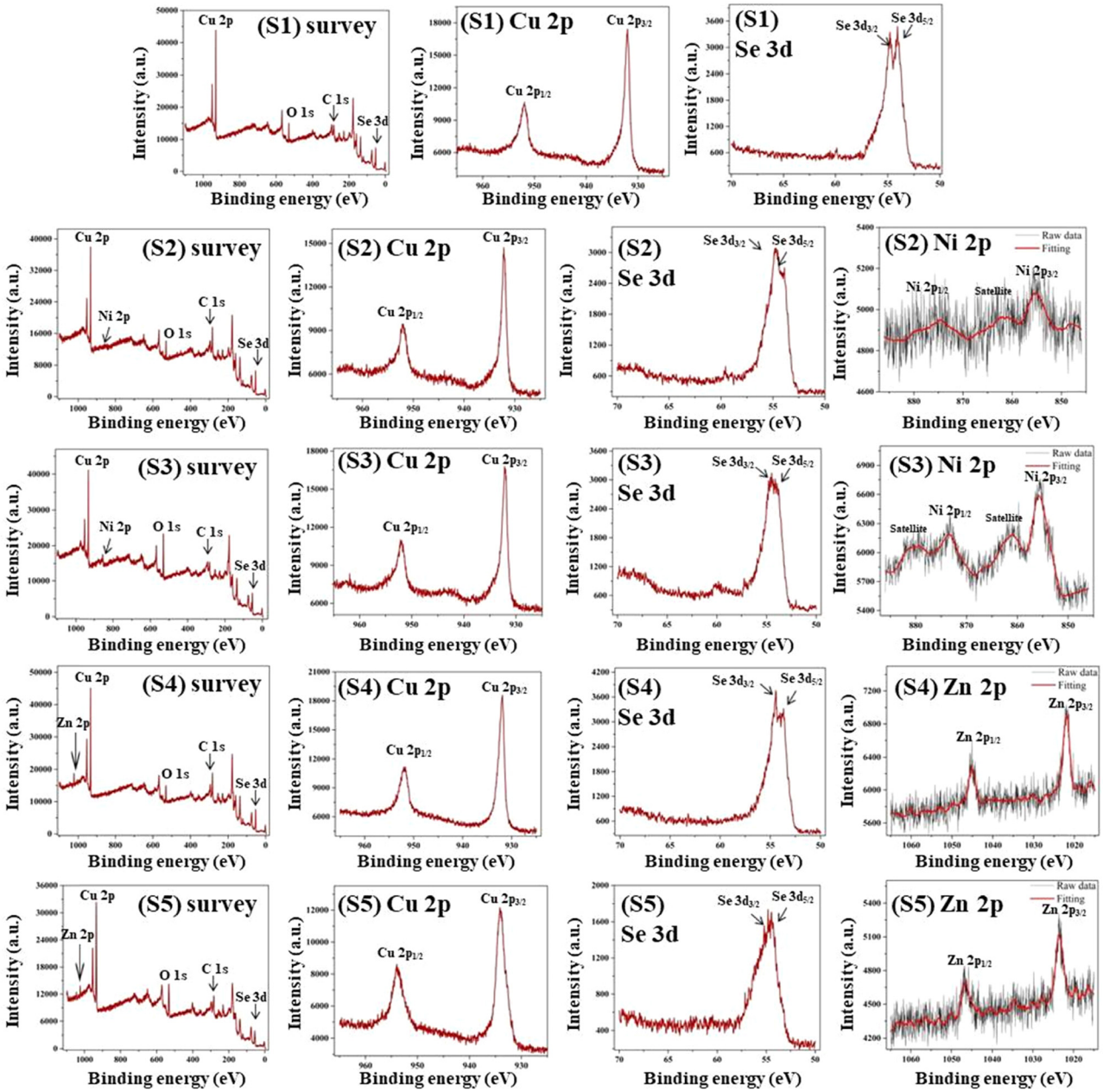

Fig. 1 The XPS spectra of as-synthesized S1–S5 nanoparticles.

both of the Cu 2p peaks and Se 3d peaks for each nanoparticle indicate the existence of CuSe.

The XPS profiles of Ni 2p for both S2 and S3 nanoparticles exhibit two signature photoelectron spikes for Ni $2p_{3/2}$ and Ni $2p_{1/2}$ with binding energies of around 855.7 and 873.4 eV, respectively.[45] Two extra spikes in the Ni 2p spectra at 862.4 and 880.2 eV can be ascribed to satellite structures of the Ni^{2+} ion.[46] The occurrence of these peaks in S2 and S3 nanoparticles evidenced the presence of Ni^{2+}. For S4 and S5 nanoparticles, the Zn 2p XPS spectra revealed two prominent bands of Zn $2p_{3/2}$ and Zn $2p_{1/2}$ with binding strengths of 1022.3 and 1045.2 eV, respectively, confirming the inclusion of the Zn^{2+} ion.[47] These results provide confirmation for Ni and Zn-doping in pristine CuSe nanoparticles and each of the identified values is congruent with the previous equivalents.

4. Thermal analysis

The TG, DTG, and DTA thermal profiles are acquired concurrently for all as-synthesized nanoparticles. The thermal measurement is performed in an inert nitrogen (N_2) gas environment at a flow rate of 100 mL each minute. The temperature profiles are recorded using a sequential series of four heating rates of 5, 10, 15, and 20 K min^{-1}. The three thermocurves are all measured throughout the range of temperatures from room temperature to 793 K.

4.1 Thermogravimetric study

Fig. 2 (a–e) portrays the TG profiles perceived for all five nanoparticles at four separate heating speeds. Referring to the TG curves, the nanoparticles undergo a two-step degradation mechanism for each of the four heating speeds. The initial phase of weight reduction is noted from ambient temperature up to 638 K, showing that all nanoparticles exhibit minuscule weight loss within this temperature interval. Alternatively, during the second stage of decomposition between 638 K and 793 K, the mass diminution is striking.

All the nanoparticles are resilient throughout the first breakdown stage, referring to the minimal weight diminution up to 638 K. Evaporation of water molecules and other weaker molecules from samples accounts for the minimal weight reductions detected within the aforementioned temperature range.[48,49]

Following the initial stage, TG profiles presented the commencement of decomposition in the second temperature range. This second temperature range shows that there are three distinct phases for the decomposition process: an initial rapid reaction, a further progressive reaction through an extended temperature range, and a last flat-end reaction. As the nanoparticles disintegrate, selenium progressively evaporates, enriching the specimens with copper and correlating the stoichiometric transition from CuSe to Cu_2Se.[27] The further validation of this phase transformation is strengthened through annealing one of the five samples, which is pristine CuSe, at 793 K under vacuum conditions. The as-synthesized pristine CuSe nanoparticles are taken within a quartz tube, which is evacuated and sealed at a vacuum level of approximately 10^{-5} Torr. The nanoparticles are subjected to annealing at 793 K in a high-temperature hot-wall furnace for 6 hours. Fig. S5 (ESI†) showcases the XRD, which elucidates the phase

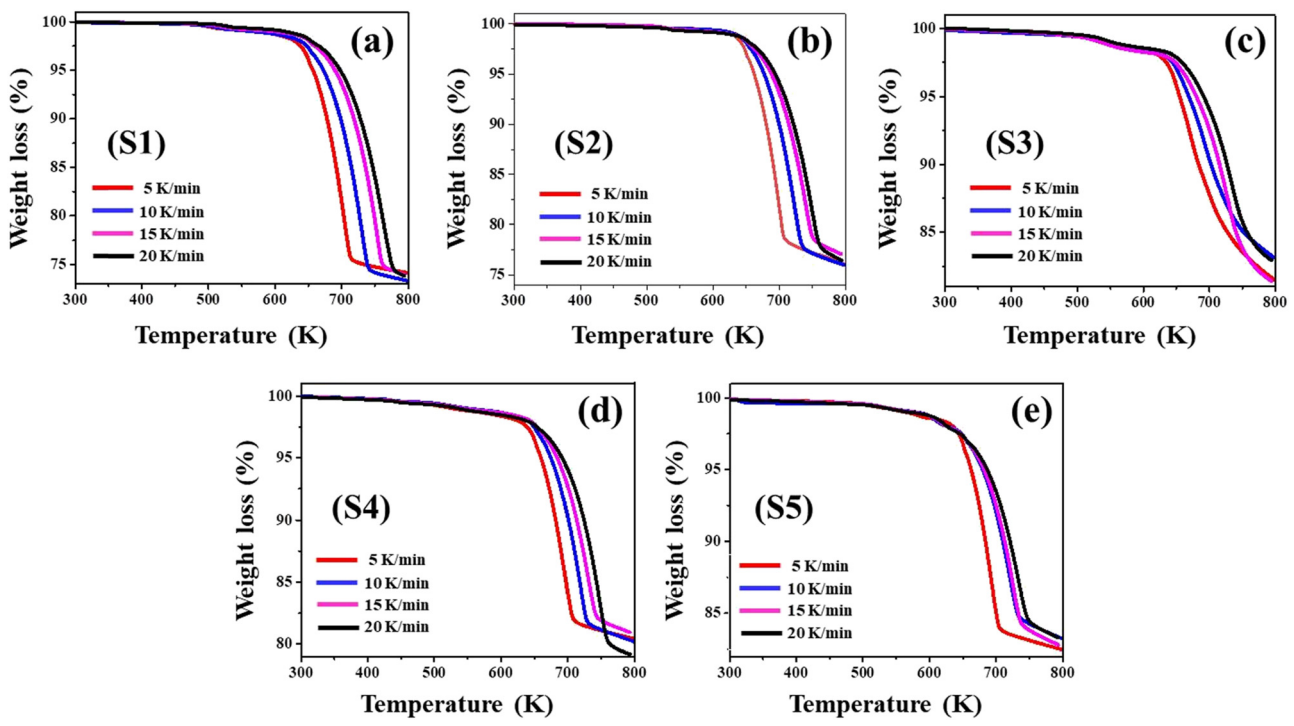

Fig. 2 The TG curves for as-synthesized S1–S5 nanoparticles.

Table 1 The temperature range and weight loss from TG curves for as-synthesized nanoparticles

		Temperature range			
		Weight loss (%)		Total weight loss (%)	
		Step-1	Step-2		
Sample	Heating rates (K min^{-1})	301–638 K	639–793 K	301–793 K	Average weight loss (%)
S1	5	2.44	23.32	25.76	26.08
	10	1.91	24.59	26.5	
	15	1.46	24.51	25.97	
	20	1.37	24.73	26.1	
S2	5	1.39	22.25	23.64	23.44
	10	1.08	22.73	23.81	
	15	1.21	21.67	22.88	
	20	1.16	22.28	23.44	
S3	5	2.68	15.57	18.25	18.18
	10	2.06	15.5	17.56	
	15	2.05	16.43	18.48	
	20	1.78	16.67	18.45	
S4	5	2.4	17.08	19.48	19.70
	10	1.87	17.78	19.65	
	15	1.75	17.23	18.98	
	20	1.89	18.81	20.7	
S5	5	2.05	15.31	17.36	16.87
	10	1.97	14.48	16.45	
	15	2.13	14.98	17.11	
	20	2.15	14.42	16.57	

transformation of the pristine CuSe nanoparticles into a cubic Cu_2Se crystal structure (JCPDS 06-0680) following the thermal annealing process.[27,50]

Table 1 lists the percentage of mass reduced along with the temperature band for each sample. As depicted in Table 1, the initial step of degradation from ambient temperature to 638 K causes no substantial reduction in weight for any of the five nanoparticles. All the nanoparticles undergo extensive weight loss within the second stage of decomposition. Based on the mean weight loss in Table 1, sample S1 lost substantially more mass (26.08%) among all other samples. For S2 and S3, this value drops to 23.44% and 18.18% respectively, while for S4 and S5, it falls to 19.70% and 16.87% respectively. These findings highlight that higher concentrations of Ni and Zn doping enhance the thermal stability of pristine CuSe nanoparticles. The weight loss data for S4 and S5 are lower than those for S2 and S3, indicating that Zn doping is more efficient regarding thermal durability than Ni doping. This can be a consequence of the greater melting point of zinc selenide as compared to nickel selenide and pristine copper selenide.[51,52]

The TG contours in Fig. 2 illustrate that the slower heating rates trailed behind the faster ones. It highlights that the overall mass losses for all samples rise with increasing heating speeds. The greater mass loss at higher heating speeds is a consequence of heat transfer constraints.[53,54] As a result of the heat transmission constraint at high heating rates, the overall temperature of the sample rises before the applied external heat has fully dissipated throughout the whole sample. At a slower rate of heating, the entire sample will dissipate heat uniformly. Uneven heat dissipation causes more mass loss in contrast to its uniform counterpart. This impact is supported by the movement of both Peak-1 and Peak-2 of the DTG graph to greater temperature values with increasing heating speed, as illustrated in Table 2.

4.2 Differential thermogravimetric (DTG) analysis

The DTG contours obtained simultaneously at four different heating rates for each sample exhibit two distinct peaks as represented in Fig. 3. All four heating rates have their peaks within the temperature range where weight reduction

Table 2 The DTG peak positions for all as-synthesized nanoparticles

	DTG peak position T_m (K)									
	S1		S2		S3		S4		S5	
Heating rates (K min^{-1})	Peak 1	Peak 2	Peak 1	Peak 2	Peak 1	Peak 2	Peak 1	Peak 2	Peak 1	Peak 2
5	504	703	511	702	523	674	500	697	508	693
10	515	731	522	725	530	695	510	720	514	721
15	527	755	528	741	535	728	517	732	522	726
20	531	764	534	750	540	735	528	749	531	734

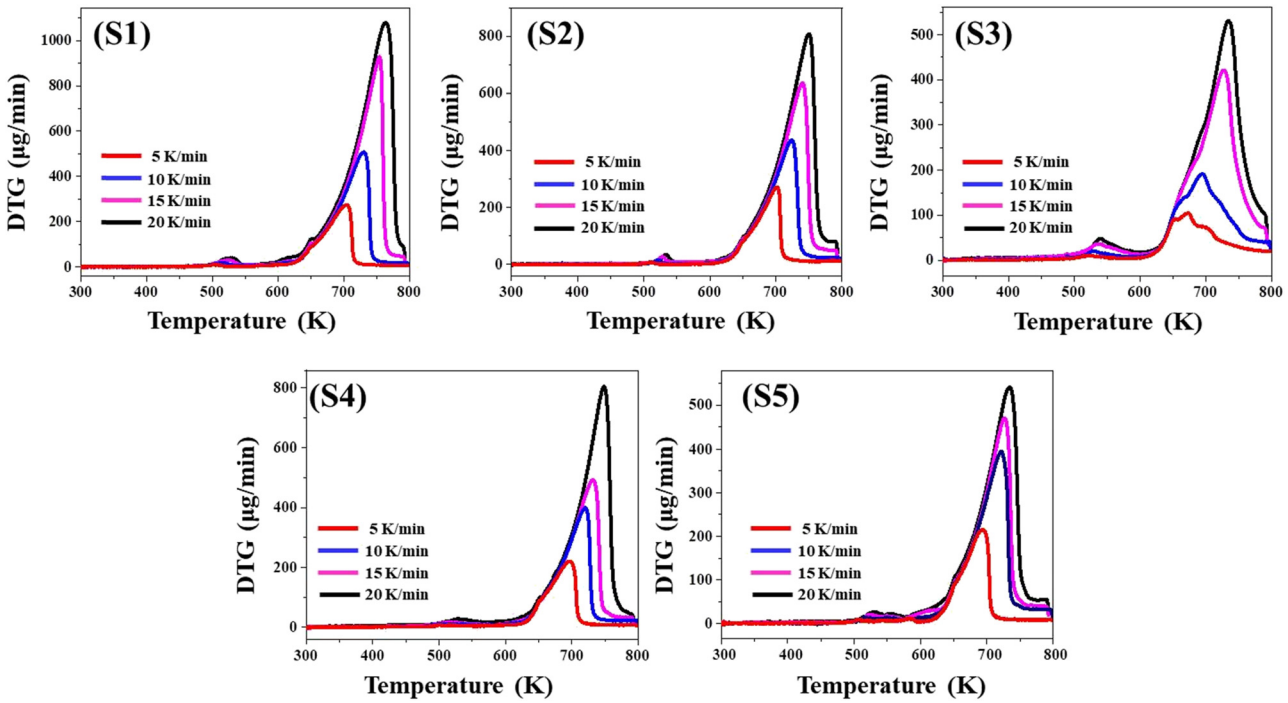

Fig. 3 The DTG curves for as-synthesized S1–S5 nanoparticles.

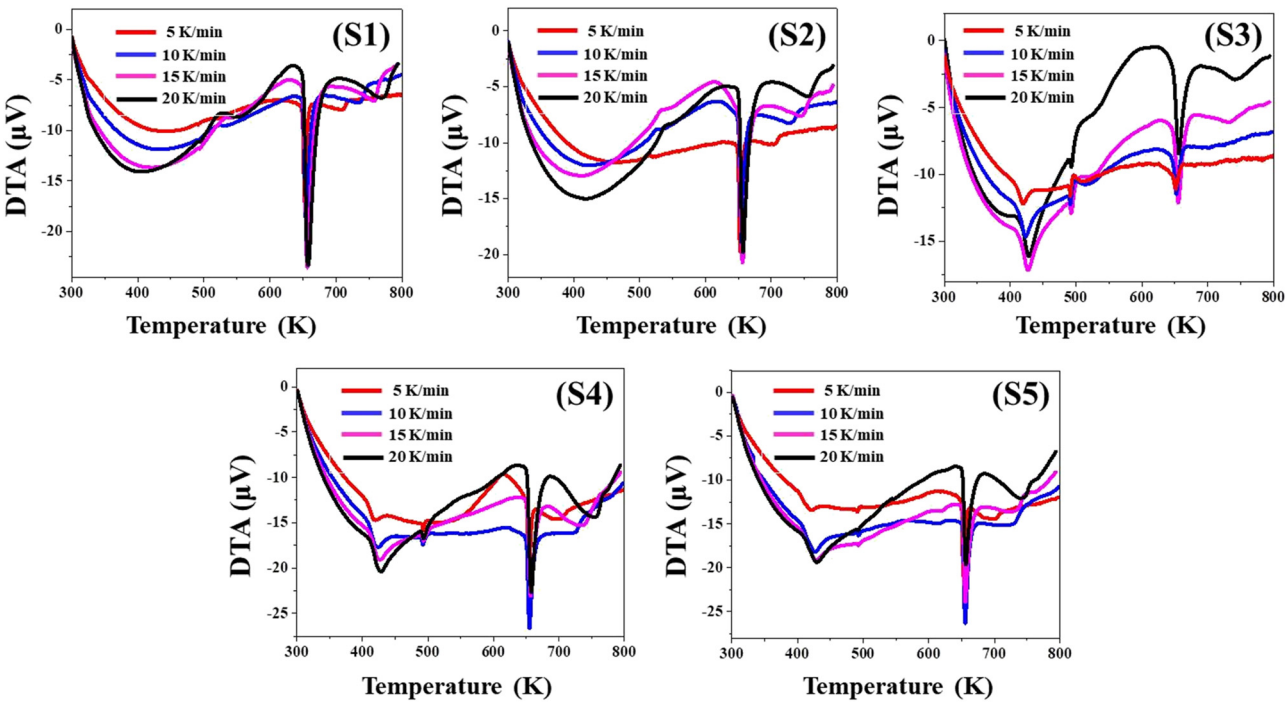

Fig. 4 The DTA profiles for as-synthesized S1–S5 nanoparticles.

is recorded for the associated TG curves. Furthermore, this finding provides support for the two-stage breakdown of all samples in TG analysis. Table 2 lists the coordinates of the DTG peaks for all samples. A close scrutiny of DTG peak locations reveals that it migrates towards higher temperature values as the heating rates increase. This is attributed to a limitation in the heat transfer characteristic, as seen in the TG curves.

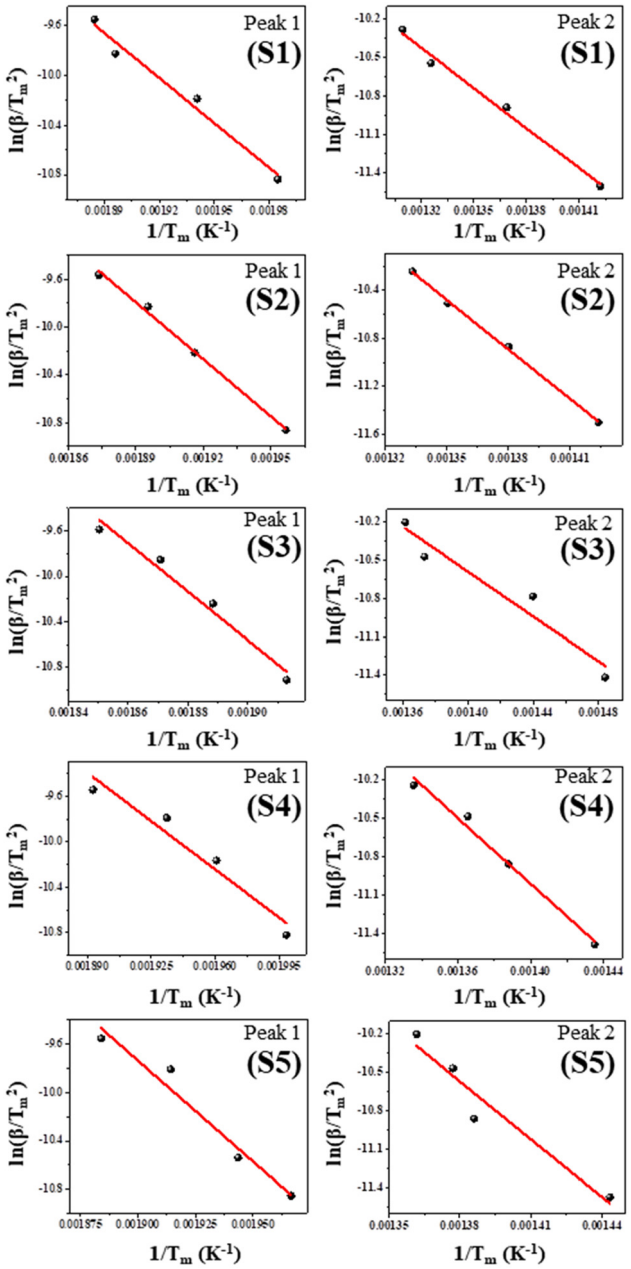

Fig. 5 Kissinger plots for as-synthesized S1–S5 nanoparticles.

4.3 Differential thermal analysis (DTA)

Fig. 4 depicts the concurrently acquired DTA profiles of the yielded nanoparticles at four distinct heating speeds. For all four heat rates examined, the DTA profiles of all the nanoparticles remain below the zero scale, indicating that they are endothermic. As a consequence of the endothermic behavior, the sample uptakes the heat, disintegrates, and eliminates volatile elements. Weight reduction in the relevant temperature range of TG graphs is evidence for the liberation of volatile elements. Previous thermal studies of pure CuSe nanoparticles have also shown comparable endothermic tendencies.[27,29]

The evaluation of the TG, DTG, and DTA contours makes it clearly evident that all the data are congruent with one another and support each of their findings.

4.4 Kinetic parameters

The thermodynamics of the yielded nanoparticles can be properly understood with the aid of the kinetic parameters. In this section, the kinetic variables are computed from the acquired thermo-curves implementing the iso-conversional linear integral Kissinger formula. The Kissinger correlation is as follows:[55]

$$\ln\frac{\beta}{T_m^2} = \ln\frac{AR}{E_a} - \frac{E_a}{RT_m} \quad (1)$$

where DTG peak temperature is denoted by T_m, R is the gas constant, and β is the heating rate. Fig. 5 displays the Kissinger maps of $\ln\frac{\beta}{T_m^2}$ against $\frac{1}{T_m}$ for two decomposition phases across all nanoparticles.

The Arrhenius factor (A) as well as activation energy (E_a) associated with as-synthesized nanoparticles are derived from the intercepts and slopes from the Kissinger maps. Implementing the estimates of A and E_a, other kinetic variables such as the activation enthalpy (ΔH^*), the activation entropy (ΔS^*), and the Gibbs free energy change (ΔG^*) are computed for all the nanoparticles.[55]

Comparison of the E_a estimates of Peak-1 for all nanoparticles reveals that S2 has a greater value than the other four samples as shown in Table 3. This finding demonstrates that S2 nanoparticles are more stable in the lower temperature range. This conclusion is supported by the lesser mass loss in Step-1 for S2 compared to all other samples, as depicted in Table 1. On the other hand, an assessment of the E_a estimates of Peak-2 for all samples demonstrates that S5 has a greater value, indicating the greater stability of S5 nanoparticles in the second temperature range. This finding is further validated by S5 experiencing less mass loss in Step-2 compared to the other samples, as seen in Table 1.

All nanoparticles attained positive ΔH^* values. These positive figures signify heat absorption in the entire thermal range. The sample decomposes as a consequence of the increase in internal energy driven by heat absorption. The TG weight loss corroborates the sample decomposition. The endothermic character of DTA profiles provides additional evidence for heat absorption by the sample. Sample S2 shows the maximum ΔH^* value in the initial temperature zone, whereas sample S5 has the highest ΔH^* value in the second temperature region. These findings are consistent with the activation energy estimates for all nanoparticles.

Entropy quantifies the extent of disorder inherent in a given system. A positive entropy change ($\Delta S^* > 0$) is typically correlated to a mass reduction resulting from the liberation of disordered or gaseous entities, which frequently aligns with the elimination of volatile constituents such as water or other compounds with low molecular weight. A negative entropy change ($\Delta S^* < 0$) is commonly associated with a weight

Table 3 The kinetic parameters evaluated from DTG curves for S1–S5 nanoparticles

Sample	Peaks	Activation energy E_a (kJ mol^{-1})	Arrhenius constant A (min^{-1})	Enthalpy ΔH^* (kJ mol^{-1})	Entropy ΔS^* (J mol^{-1})	Gibbs energy ΔG^* (kJ mol^{-1})
S1	Peak 1	99.65	5.25×10^9	95.33	−63.46	128.28
	Peak 2	86.48	2.83×10^5	80.34	−148.10	189.65
S2	Peak 1	176.99	2.03×10^{17}	172.63	81.74	129.83
	Peak 2	73.00	4.81×10^4	66.93	−162.74	185.64
S3	Peak 1	132.31	1.03×10^{13}	127.89	−0.64	128.23
	Peak 2	114.18	4.34×10^7	108.29	−105.91	183.25
S4	Peak 1	112.11	1.34×10^{11}	107.72	−36.43	126.44
	Peak 2	106.69	1.35×10^7	100.66	−115.84	184.60
S5	Peak 1	138.46	5.43×10^{13}	134.15	12.09	126.79
	Peak 2	124.90	3.89×10^8	118.93	−87.80	182.03

reduction caused by the generation of more ordered or compacted products.[56]

As shown in Table 3, the ΔS^* values in Step-1 are greater, but the values in Step-2 are negative. The entropy (ΔS^*) values demonstrate a direct relationship with E_a and A; as the values of E_a and A increase, so do the values of (ΔS^*).[57] The equilibrium between these variables dictates the overall kinetics of the reaction. As depicted in Table 3, the positive ΔS^* values for Peak-1 in samples S2 and S5 align with the greater activation energy for the same. A reaction featuring elevated activation energy values for S2 and S5 during the initial stage signifies the demand for more energy input for the sample to reach the transition state. These observations suggest that the sample decomposition leads to products with higher disorder, resulting in a positive change in entropy. The noted negative entropy values in the second step across all specimens signify that the ultimate products exhibit a greater degree of order and thermal stability compared to the initial state.

The ΔG^* values are positive in every stage and for all samples. Positive values for ΔG^* signify that the decomposition mechanism is not spontaneous. The degradation of the sample *via* heat absorption is justified by all of the observed and obtained thermodynamic parameters, which are all in accordance with one another.

5. Computational characterization

Density functional theory (DFT) implemented in the Quantum Espresso package[58] is used to evaluate the phonon dynamics stability of CuSe with doping of Ni and Zn in the Cu site. The exchange–correlation energy is estimated using the Perdew–Burke–Ernzerhof method under the framework of the generalized gradient approximation.[59,60] The plane-wave kinetic energy cutoff is 550 eV, and the Brillouin zone is sampled using a (12 × 12 × 6) k-point grid in the Monkhorst–Pack technique.[61] The computations are carried out after attaining energy and atom force convergence criteria of 0.001 eV Å^{-1} and 10^5 eV, respectively, for both lattice parameters and atom locations.[62]

5.1 Structural properties

Fig. 6(a–c) illustrate the CuSe covellite that exhibits a hexagonal $P6_3/mmc$ space group. Cu^{1+} is bound to one Se^2 and three equivalent Se^{1-} atoms to produce Ni, Zn/$CuSe_4$ tetrahedra, with three equivalent $SeCu_3Se$ tetrahedra and seven equivalent Ni, Zn/$CuSe_4$ tetrahedra sharing corners. Cu^{2+} is linked to three equivalent Se_2 atoms in a trigonal planar shape. The length of all Ni, Zn/Cu–Se bonds is 2.32 Å. Se^1 is bound to three equivalent Ni^{1+}, Zn^{1+}/Cu^{1+} and one Se^1 atom to produce distorted $SeCu_3Se$ tetrahedra with three equivalent Ni, Zn/$CuSe_4$ tetrahedra, six equivalent $SeCu_3Se$ tetrahedra, and three equivalent $SeCu_5$ trigonal bipyramids. The length of the Se–Se bond is 2.43 Å. Se^2 is coupled to two equivalent Cu^{1+} and three

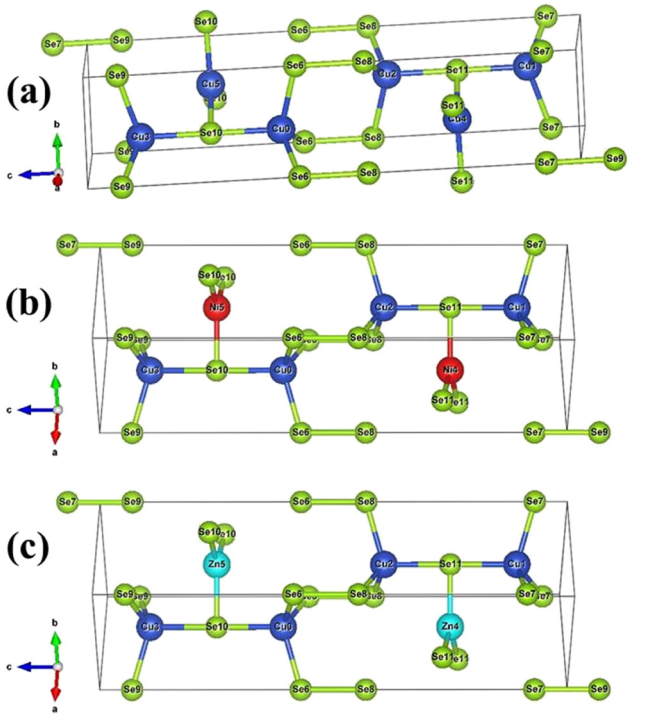

Fig. 6 The crystal structure of (a) pristine CuSe (Cu in blue and Se in green color), (b) Ni:CuSe (Ni in red color) and (c) Zn:CuSe (Zn in light blue color).

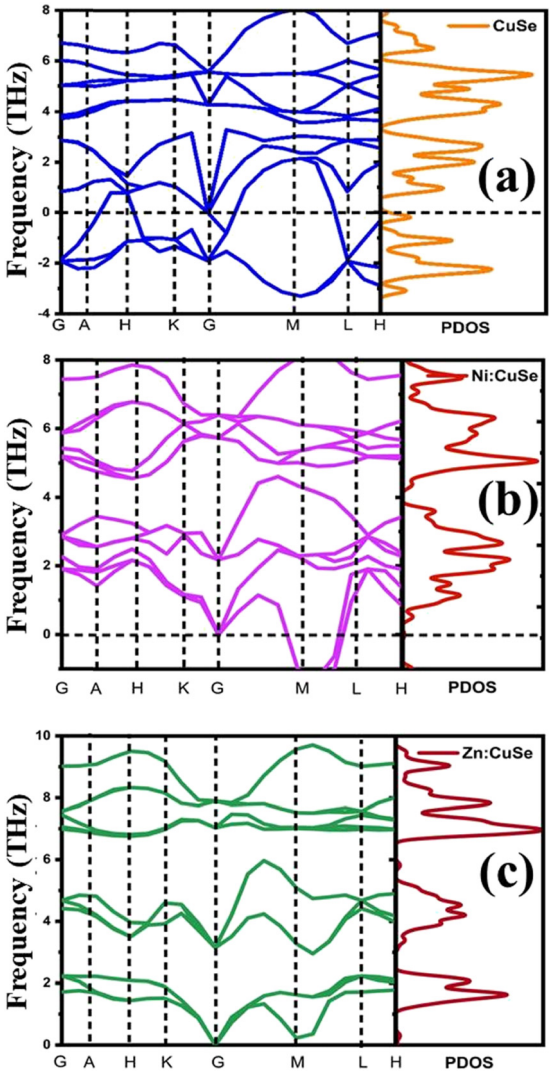

Fig. 7 Phonon dynamics in the high symmetric point for (a) pristine CuSe, (b) Ni:CuSe, and (c) Zn:CuSe hexagonal nanoparticles.

equivalent Cu^{2+} atoms to create $SeCu_5$ trigonal bipyramids with six equivalent $SeCu_3Se$ tetrahedra and six equivalent $SeCu_5$ trigonal bipyramids.

5.2 Phonon dynamic stability

The assessment of the dynamic stability of pristine CuSe as well as Ni and Zn-doped CuSe nanoparticles with a hexagonal structure involves an examination of the phonon dispersion curve and the phonon density of states (DOS), as depicted in Fig. 7(a–c). For pure CuSe (Fig. 7a), the existence of modes exhibiting negative phonon frequency values indicates a certain level of dynamic instability. When a Ni atom is introduced as a dopant on the Cu side, the phonon stability improves compared to the pure CuSe compound, as depicted in Fig. 7b. Moreover, upon the introduction of Zn atoms on the Cu side, the phonon dynamics achieved an even higher level of stability, characterized by the absence of negative phonon frequencies, as illustrated in Fig. 7c. The enhanced phonon dynamic stability in Zn-doped CuSe nanoparticles aligns with the greater thermal stability observed in the TG study (Section 4.1) in comparison to both pristine CuSe and Ni-doped CuSe nanoparticles. The number of potential vibrational orientations in a system is denoted by $d(N-1)$, with N representing the number of atoms in a unit cell, determining the number of optical modes. Vibrations along the bond axis are called longitudinal polarization, while those perpendicular to this axis are termed transverse polarization. A total of 12 vibration modes are identified in the hexagonal crystal systems of pristine CuSe as well as Ni and Zn-doped CuSe, each containing 4 atoms per cell and consisting of 4 acoustic and 8 optical modes.

The phonon dispersion curves and phonon density for nanoparticles of pristine CuSe and those doped with Ni and Zn are conducted along the high-symmetry points *G–A–H–K–G–M–L–H* (Fig. 7), utilizing a frequency range from −5 to 10 THz under the ground state conditions ($P = 0$ GPa). Within the lowest frequency range, there are four acoustic branches, whereas the remaining eight branches belong to the higher frequency range. The *–X* direction features two-fold degenerate transverse acoustic modes, while at points *G*, *H*, and *M*, there is an overlap between the acoustic and optical branches in both pristine and Ni- and Zn-doped CuSe nanoparticles. At the *A-H* point, there are four doubly degenerate optical modes, with the corresponding band gaps of approximately 1.20 and 2.5 THz wide. The phonon DOS extends from 0 to 3 THz and is primarily associated with vibrations involving the cation Cu/Ni/Zn and the anion Se. The phonon DOS at roughly 0 to 4 THz range is primarily attributed to Se anion vibrations, with a significant contribution from the Cu (Ni/Zn) cation. Beyond 4.5 THz, Cu and Se vibrations predominantly contribute to the phonon DOS, with minor contributions from the Ni and Zn cations.

6. Thermoelectric properties

Investigations of electrical and thermal transport characteristics are conducted on pellets made of the nanoparticles *via* hydraulic pressing. Hydraulic compressing of an equally filled powder of individual nanoparticles into a die (pelletizer) at a pressure of 0.9 GPa over 30 minutes produces pellets of pristine CuSe as well as Ni- and Zn-doped CuSe nanoparticles. The resulting pellets have a circumference of 1.4 cm and an average thickness of 1 mm.

6.1 Thermoelectric power

The temperature dependence of the potential variance between the two probes was studied across the range of 300 K to 523 K on pellets produced from pristine CuSe and Ni- and Zn-doped CuSe nanoparticles. The correlation between the Seebeck coefficient '*S*' and inverse of temperature (1000/*T*) for each sample is demonstrated in Fig. 8. Throughout the full temperature range, the thermoelectric power (TEP) of each specimen appears positive, indicating their p-type semiconducting character. The characteristic semiconducting nature of all nanoparticles is confirmed by the steady fall of the value of '*S*' with the increasing value of (1000/*T*). Moreover, the positive indication of the TEP value remains unchanged with increasing

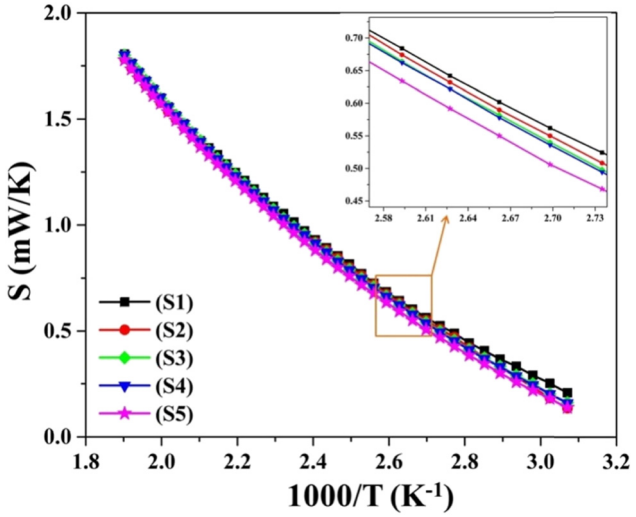

Fig. 8 Variation of thermoelectric power *versus* inverse of temperature for as-synthesized S1–S5 nanoparticles.

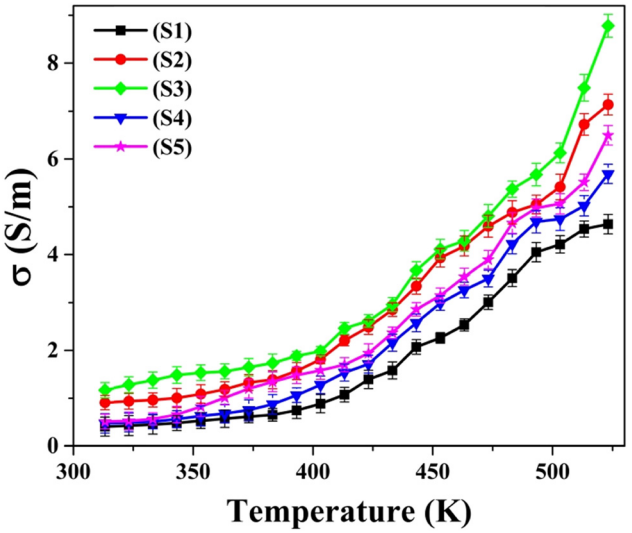

Fig. 9 Variation of dc electrical conductivity with temperature for as-synthesized S1–S5 nanoparticles.

temperature for all samples. This indicates that there is no phase change in any of the materials throughout the whole investigated temperature range. As elucidated in Fig. 8, the alteration of '*S*' as a function of the reciprocal of temperature exhibits an almost consistent uniformity across all the nanoparticles. For more precise differentiation of the temperature-dependent behavior of '*S*' across each sample, Fig. 8 presents a magnified inset of a smaller domain. Throughout the entire temperature span, it is evident that Zn-doped CuSe exhibits a lower magnitude of "*S*" compared to Ni-doped CuSe nanoparticles. The decrement in the Seebeck coefficient (S) values ascertained for Zn-doped CuSe and Ni-doped CuSe samples can be attributed to the dissimilarity in ionic radii between the Zn^{2+} dopant ion and the Ni^{2+} dopant ion compared to the host Cu^{2+} ion.[41,63] A greater disparity in ionic radii between Zn^{2+} and Cu^{2+} ions leads to a more pronounced strain within the S4 and S5 samples, as corroborated by the detailed XRD examination of identical nanoparticles in the authors' recent publication.[41] The microstrain data extracted from XRD data evaluation, as detailed in Table S4 (ESI†), definitively corroborate the higher degree of strain in Zn-doped CuSe nanoparticles relative to their Ni-doped CuSe counterparts. The presence of strain impedes and forms a hindrance to the unimpeded mobility of the majority charge carriers, consequently leading to a diminution in the "*S*" value. The standard formula given below is employed to get the Fermi energy (E_f) and the scattering parameter (s) for each nanoparticle:[64]

$$S = \frac{K_B}{e}\left[A + \frac{E_f}{K_B T}\right] \quad (2)$$

In this instance, K_B denotes the Boltzmann constant, e the electronic charge, A the constant defined by the dominant scattering mechanism, and E_f the distance between the Fermi level and the top of the valence band. The scattering constant A is calculated *via* the slope of Fig. 6(b), and the effective scattering energy E_f is calculated using the intercept. The scattering parameter (s) is computed from $s = 5/2 - A$.[64] The outcomes are summarized in Table 4.

Table 4 The estimated E_f, A, and s values for as-synthesized S1–S5 nanoparticles

Sample	E_f	A	s
S1	1.43	4.39	−1.89
S2	1.41	4.36	−1.86
S3	1.40	4.34	−1.84
S4	1.38	4.31	−1.81
S5	1.37	4.29	−1.79

Table 4 demonstrates that Ni- and Zn-doped CuSe nanoparticles exhibit lower Fermi energies (E_f) than pristine CuSe nanoparticles. As described by Zoater *et al.*, E_f values indicate the distance from the Fermi level to the top of the valence band.[65] The minor drop in the E_f value with increasing Ni and Zn doping in pure CuSe validates the fact that Ni and Zn-doped nanoparticles are less resistive than pristine CuSe. All nanoparticles exhibit negative values for their scattering parameter (s), indicating that the scattering process results from carrier scattering by acoustic phonons in a single parabolic band model.[64]

6.2 Electrical conductivity

Fig. 9 graphically elucidates the alteration in dc electrical conductivity 'σ' as a function of temperature across the temperature span extending from ambient temperature to 523 K. The graph portrays a proportional elevation in σ values with increasing temperature, offering validation for the semiconducting characteristics of all five as-synthesized nanoparticles. These findings substantiate the semiconductor properties of all five nanoparticles, as evident in the temperature-dependent variation of '*S*'. The enhancement of electrical conductivity (σ) is concurrently discerned alongside the increasing concentrations of Ni and Zn dopants within CuSe nanoparticles. This rise

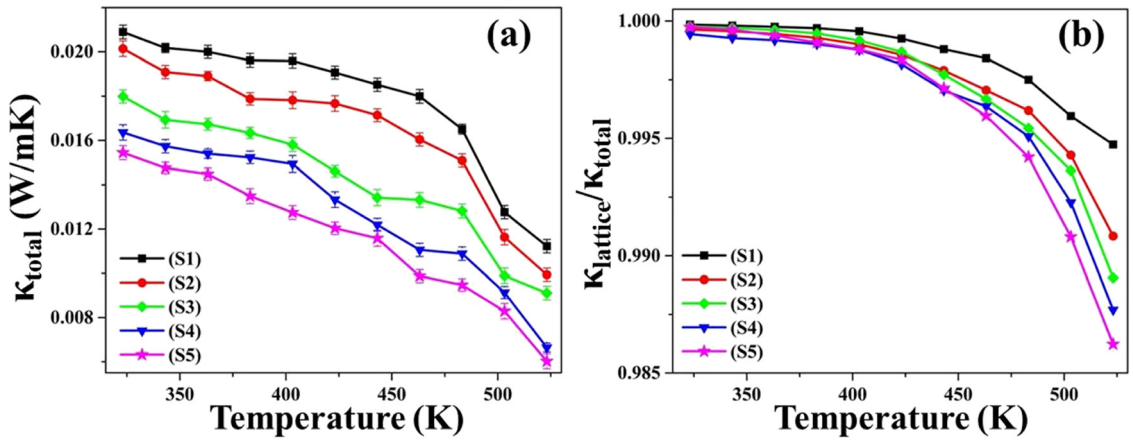

Fig. 10 The plots of (a) K_{total} *versus* temperature and (b) $K_{lattice}/K_{total}$ *versus* temperature for as-synthesized S1–S5 nanoparticles.

in 'σ' values can be linked to the increase in carrier concentration resulting from the incorporation of Ni and Zn dopants. As evident in Fig. 9, the magnitude of σ is higher for Ni-doped CuSe nanoparticles in comparison to both Zn-doped and pristine CuSe nanoparticles. The reduced magnitude of σ pertaining to Zn-doped CuSe is attributed to the increased structural strain within 5% and 10% Zn-doped nanoparticles, a phenomenon substantiated by the XRD and thermoelectric studies. The presence of strain increases the obstruction to the unhindered movement of carriers, resulting in a diminished value of σ.[63]

6.3 Thermal conductivity

Fig. 10(a) portrays the ascertained data points of total thermal conductivity (κ_{total}) plotted against temperature, encompassing the entire temperature range of 323 K to 523 K for all five as-synthesized nanoparticles. For all the samples, the thermal conductivity values exhibited a decrement with increasing temperature. The diminishment in total thermal conductivity with increasing temperature can be attributed to the occurrence of Umklapp scattering, during which phonon–phonon interaction gets more prevalent with increasing temperature.[63] The graphical depiction also reveals that, within the prescribed temperature domain, the κ_{total} magnitude is highest for pristine CuSe nanoparticles when compared to the other Ni and Zn-doped CuSe nanoparticles. The decrement in thermal conductivity witnessed in samples S2–S5 can be attributed to the structural imperfections induced by the substitution of Cu with Ni and Zn atoms.[66] This phenomenon can be ascribed to the dominant impact of phonon scattering on the metallic particles.[67] The heightened structural distortion in Zn-doped CuSe is accountable for the lowest thermal conductivity observed for 10% Zn CuSe nanoparticles.

The total thermal conductivity considers contributions primarily from the mobility of carriers and the lattice vibrations, which can be written as[68]

$$\kappa_{total} = \kappa_c + \kappa_{lattice} \quad (3)$$

where κ_c is the carrier thermal conductivity and $\kappa_{lattice}$ is the lattice thermal conductivity. The computation of the ($\kappa_{lattice}/\kappa_{total}$) ratio, which signifies the proportion of lattice to total thermal conductivity, is determined utilizing eqn (3). Fig. 10(b) displays the graph of ($\kappa_{lattice}/\kappa_{total}$) *versus* temperature within the temperature span from 323 K to 523 K. The graph depicts a gradual reduction in the ($\kappa_{lattice}/\kappa_{total}$) value as temperature rises.

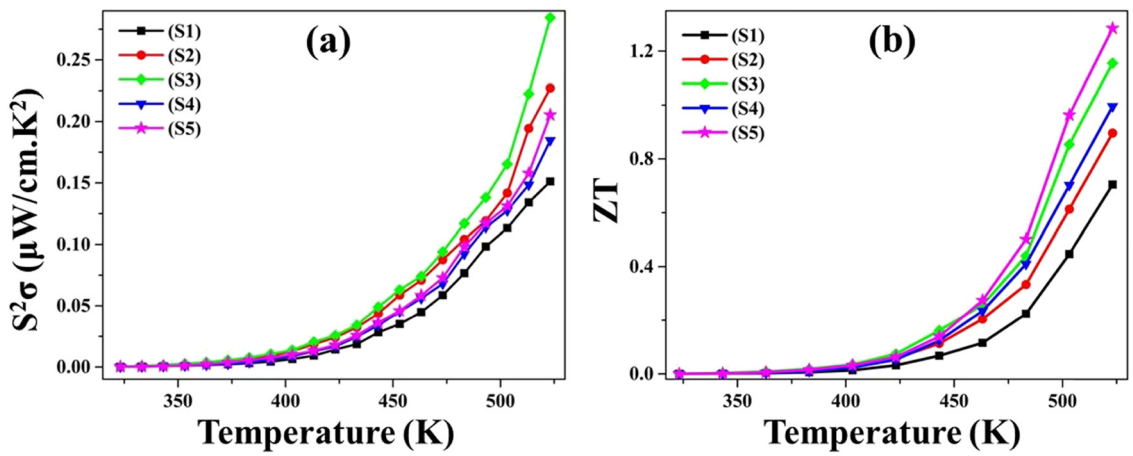

Fig. 11 The (a) power factor $S^2\sigma$ and (b) figure of merit ZT variation with temperature for as-synthesized S1–S5.

Table 5 Comparison of *ZT* for as-synthesized CuSe and 10% Zn doped CuSe with those of various chalcogenide compounds

Material	*ZT* (K)	Ref.
CuSe	0.70 at 523	This work
$Cu_{0.9}Zn_{0.1}Se$	1.28 at 523	This work
CuSe	0.021 at 423	40
$Cu_{1.98}Ni_{0.02}Se$	0.8 at 650	67
$CuSbSe_2$	0.24 at 623	69
Cu_2Se	2.1 at 973	70
$Cu_2Se_{0.98}Te_{0.02}$	1.76 at 850	71
$Cu_{1.98}Se$	1.4 at 850	72
$CuFeSe_2$	0.22 at 653	73
$Cu_{2-x}Se$–Na	0.24 at 673	74

The plot further highlights that the lattice contribution ($\kappa_{lattice}/\kappa_{total}$) decreases with the incorporation of Ni and Zn dopants into CuSe nanoparticles. The most minimal values are obtained for 5% and 10% Zn-doped CuSe nanoparticles, which can be linked to the presence of a more pronounced lattice strain.

6.4 Power factor and *ZT*

Fig. 11(a) displays the alteration of the power factor ($S^2\sigma$) as a function of temperature (T) across all five as-synthesized samples, covering the temperature domain from 323 K to 523 K. The graph illustrates that, among all examined samples, the pristine CuSe sample manifests the most minimal $S^2\sigma$ value. The increased power factor values discerned in Ni- and Zn-doped CuSe samples are attributed primarily to the increased electrical conductivity for doped samples in Fig. 9. The figure of merit (*ZT*) provides a quantification of the efficacy of the thermoelectric materials. The *ZT* value exhibits a proportionate relationship with the power factor ($S^2\sigma$) and is expressed as[68]

$$ZT = \frac{S^2\sigma}{\kappa}T \quad (4)$$

Here κ represents the total thermal conductivity. Fig. 11(b) depicts the graphical representation of *ZT versus* temperature across the temperature spectrum from 323 K to 523 K for all five as-synthesized nanoparticles. As the graph elucidates, the *ZT* values for all specimens demonstrate increment with increasing temperature. The *ZT* value acquired for pristine CuSe is 0.7 at 523 K, which represents a significant increase compared to the reported value of 0.021 for CuSe by Longbin Li *et al.*[40] As demonstrated in the plot, the *ZT* value exhibits enhancement for Ni- and Zn-doped CuSe nanoparticles when compared to pristine CuSe nanoparticles. The highest *ZT* value of 1.28 is acquired for 10% Zn-doped CuSe nanoparticles, which can be attributed to their lower total thermal conductivity, as demonstrated in Fig. 10(a). Hence, it can be posited that Ni and Zn doping in pristine CuSe nanoparticles elicits an enhancement in the thermoelectric power factor and figure of merit, thereby increasing their potential for utilization in the thermoelectric conversion domains. Table 5 presents a juxtaposition of the present data with previously documented thermoelectric results involving various chalcogenide compounds. The as-synthesized Ni and Zn-doped CuSe nanoparticles exhibit favorable outcomes when compared to other chalcogenides.

7. Conclusion

The chemical compositions of the as-synthesized nanoparticles are evidenced by XPS binding energy analysis, which affirmed the inclusion of Ni atoms in Ni-doped CuSe nanoparticles and the inclusion of Zn atoms in Zn-doped CuSe nanoparticles. All as-synthesized nanoparticles revealed a two-step breakdown through their TG curves from room temperature to 793 K, which is demonstrated by the appearance of two distinct DTG peaks in the same temperature band. TG examination proved that all nanoparticles are resilient at temperatures varying from ambient temperature to 638 K with only a negligible amount of mass loss. All nanoparticles consistently lost mass above their stability temperature, indicating that they decomposed in a single step at that temperature. Mass loss estimated from TG profiles demonstrated improved thermal stability for both Ni and Zn-doped CuSe nanoparticles, with Zn-doped nanoparticles functioning superior to Ni-doped nanoparticles. The enhanced thermal stability of Zn-doped CuSe nanoparticles is supported by the theoretical analysis of the favorable phonon dynamic stability through the DFT simulations, which demonstrate positive phonon stability. The endothermic character of DTA contours for all samples verified heat absorption that resulted in the breakdown of the samples, which is corroborated by the TG weight reduction. The non-mechanistic Kissinger correlation is utilized to estimate the kinetic variables. During decomposition, positive values of ΔH^* represent heat absorption, whereas negative values of ΔS^* demonstrate rearrangement of the structure. Positive results for ΔG^* prove that the disintegration process is not spontaneous for all as-synthesized nanoparticles. The computed kinetic statistics are consistent with all the thermocurve measurements. The variations in thermoelectric power (S) and dc electrical conductivity (σ) with temperature affirmed the p-type semiconducting attributes for all nanoparticles. All nanoparticles exhibited a temperature-dependent reduction in total thermal conductivity. The data revealed that, in terms of thermal contribution, the lattice component exerts greater dominance than the carrier contribution. The enhanced thermoelectric power factor ($S^2\sigma$) and figure of merit (*ZT*) for Ni- and Zn-doped CuSe nanoparticles confirmed an improvement in the thermoelectric performance of pristine CuSe *via* Ni and Zn doping. This study offers significant insights concerning the basic mechanisms dictating the thermal and thermoelectric characteristics of nanoparticles and validates the broad variety of potential future uses for both as-synthesized pure and Ni- and Zn-doped CuSe nanoparticles, including in high-tech thermoelectric devices, energy-efficient gadgets, energy harvesting, and many more.

Author contributions

SRP contributed to the material preparation, data collection, analysis, and writing of the original draft. SHC acquired resources, and assisted in project administration, conceptualization, and supervision. MBS contributed to data analysis and methodology. RMK participated in the formal calculation and

drafting of the manuscript. ZRP contributed to the investigation and data analysis. AJK assisted in the review and editing of the manuscript. MPD participated in the investigation and review of the manuscript.

Conflicts of interest

There are no conflicts to declare.

Acknowledgements

All the authors are thankful to the Materials Research Center, MNIT Jaipur, India, for XPS analysis of the samples.

References

1 S. E. Sheela, R. Sekar, D. K. Maurya, M. Paulraj and S. Angaiah, *Mater. Sci. Semicond. Process.*, 2023, **156**, 107273.
2 C. Lamiel, I. Hussain, H. Rabiee, O. R. Ogunsakin and K. Zhang, *Coord. Chem. Rev.*, 2023, **480**, 215030.
3 T. Eisa, M. A. Abdelkareem, D. A. Jadhav, H. O. Mohamed, E. T. Sayed, A. G. Olabi, P. Castaño and K. J. Chae, *Prog. Energy Combust. Sci.*, 2023, **94**, 101044.
4 Y. Bai, L. Sun, Q. Yu, Y. Lei and B. Liu, *Nano Res. Energy*, 2023, **2**, e9120043.
5 V. Pathak, P. Lad, A. B. Thakkar, P. Thakor, M. P. Deshpande and S. Pandya, *Results Surf. Interfaces*, 2023, **11**, 100111.
6 A. J. Khimani, S. H. Chaki, S. M. Chauhan, A. V. Mangrola, R. R. Meena and M. P. Deshpande, *Nano-Struct. Nano-Objects*, 2019, **18**, 100286.
7 M. K. Agarwal, P. D. Patel, H. Chaki and D. Lakshminarayana, *Bull. Mater. Sci.*, 1998, **21**, 291–295.
8 Y. R. Jeong, I. H. Kim and Y. J. Jeong, *Mater. Today Commun.*, 2023, **35**, 106324.
9 S. Arora, S. Chuhadiya, D. Suthar, S. Himanshu, M. S. Dhaka and G. Sharma, *J. Mater. Sci.: Mater. Electron.*, 2023, **34**, 1–9.
10 C. Zhao, W. Xu, J. Ren, L. He, C. Wu, W. Jia, D. Ye, H. Zhou, C. Hu, T. Yu, X. Luo and C. Yuan, *Inorg. Chem.*, 2022, **61**, 14455–14461.
11 I. G. Shitu, K. K. Katibi, L. S. Taura, A. Muhammad, I. M. Chiromawa, S. B. Adamu and S. G. Durumin Iya, *Ceram. Int.*, 2023, **49**, 12309–12326.
12 S. A. Ahmad, M. Z. U. Shah, M. Arif, E. Ullah, S. ur Rahman, M. S. U. Shah, S. M. Eldin, P. Song, M. Sajjad and A. Shah, *Ceram. Int.*, 2023, **49**, 20007–20016.
13 H. Fu, A. Zhang, H. Guo, L. Duan, F. Jin, H. Zong, X. Sun and J. Liu, *ACS Appl. Mater. Interfaces*, 2023, **15**, 8169–8180.
14 K. Giribabu, R. Suresh, R. Manigandan, E. Thirumal, A. Stephen and V. Narayanan, *J. Mater. Sci.: Mater. Electron.*, 2013, **24**, 1888–1894.
15 K. S. Urmila, T. N. Asokan, R. R. Philip, V. Ganesan, G. S. Okram and B. Pradeep, *Phys. Status Solidi Basic Res.*, 2014, **251**, 689–696.
16 H. Zou, L. Gong, Y. Xu, H. Ni, Y. Jiang, Y. Li, C. Huang and Q. Liu, *Talanta*, 2023, **261**, 124663.
17 Y. Mao, H. Zou, Q. Wang and C. Huang, *Sci. China: Chem.*, 2016, **59**, 903–909.
18 C. Hu, Z. Zhang, S. Liu, X. Liu and M. Pang, *ACS Appl. Mater. Interfaces*, 2019, **11**, 23072–23082.
19 N. I. Akpu, A. D. Asiegbu, L. A. Nnanna, I. L. Ikhioya and T. I. Mgbeojedo, *J. Mater. Sci.: Mater. Electron.*, 2022, **33**, 1154–1161.
20 V. R. Voggu, J. Sham, S. Pfeffer, J. Pate, L. Fillip, T. B. Harvey, R. M. Brown and B. A. Korgel, *ACS Energy Lett.*, 2017, **2**, 574–581.
21 K. Murtada, R. Salghi, A. Ríos and M. Zougagh, *J. Electroanal. Chem.*, 2020, **874**, 114466.
22 X. Jiang, S. Zhang, F. Ren, L. Chen, J. Zeng, M. Zhu, Z. Cheng, M. Gao and Z. Li, *ACS Nano*, 2017, **11**, 5633–5645.
23 S. M. Chauhan, S. H. Chaki, M. P. Deshpande, J. P. Tailor, A. J. Khimani and A. V. Mangrola, *Nano-Struct. Nano-Objects*, 2018, **16**, 200–208.
24 S. Masrat, R. Poolla, P. Dipak and M. B. Zaman, *Surf. Interfaces*, 2021, **23**, 100973.
25 A. K. Keyan, D. Vasu, S. Sakthinathan, T. W. Chiu, Y. H. Lee and C. C. Lin, *Electrocatalysis*, 2023, **14**, 448–462.
26 N. I. Akpu, A. D. Asiegbu, L. A. Nnanna, I. L. Ikhioya and T. I. Mgbeojedo, *J. Mater. Sci.: Mater. Electron.*, 2022, **33**, 1154–1161.
27 G. Niu, J. Lu, X. Wang, B. Wang, X. Liu, Z. Liu, Y. Zhuang, Y. Que, C. Xu, J. Ying Chyi Liew, Z. Abidin Talib, Z. Zainal, M. Ahmad Kamarudin, N. Huda Osman and H. Kee Lee, *Semicond. Sci. Technol.*, 2019, **34**, 125017.
28 I. G. Shitu, Z. A. Talib, J. L. Y. Chi, M. M. A. Kechick and H. Baqiah, *Results Phys.*, 2020, **17**, 103041.
29 H. Luo, H. Xiong, W. Long Jiang, L. Liu, G. Zheng Zha, T. Tian Zhen, B. Yang and B. Qiang Xu, *Trans. Nonferrous Met. Soc. China*, 2022, **32**, 3478–3486.
30 C. D. Jadhav, S. R. Rondiya, R. C. Hambire, D. R. Baviskar, A. V. Deore, R. W. Cross, N. Y. Dzade and P. G. Chavan, *J. Alloys Compd.*, 2021, **875**, 159987.
31 M. Råsander, L. Bergqvist and A. Delin, *J. Phys.: Condens. Matter*, 2013, **25**, 125503.
32 Y. Zhang, Y. Wang, L. Xi, R. Qiu, X. Shi, P. Zhang and W. Zhang, *J. Chem. Phys.*, 2014, **140**, 074702.
33 G. Chen, M. S. Dresselhaus, G. Dresselhaus, J. P. Fleurial and T. Caillat, *Int. Mater. Rev.*, 2013, **48**, 45–66.
34 X. L. Shi and Z. G. Chen, *Joule*, 2023, **7**, 1108–1110.
35 S. Sun, M. Li, X. L. Shi and Z. G. Chen, *Adv. Energy Mater.*, 2023, **13**, 2203692.
36 M. Yao, W. Liu, X. Chen, Z. Ren, S. Wilson, Z. Ren and C. Opeil, *J. Alloys Compd.*, 2017, **699**, 718–721.
37 D. Yang, X. Su, J. Li, H. Bai, S. Wang, Z. Li, H. Tang, K. Tang, T. Luo, Y. Yan, J. Wu, J. Yang, Q. Zhang, C. Uher, M. G. Kanatzidis and X. Tang, *Adv. Mater.*, 2020, **32**, 2003730.
38 Z. Geng, D. Shi, L. Shi, Y. Li, G. J. Snyder and K. Ho Lam, *J. Mater*, 2019, **5**, 626–633.
39 F. Kong, J. Bai, P. Bi, X. Liu, Z. Wang and R. Xiong, *Ceram. Int.*, 2019, **45**, 8866–8872.
40 L. Li, Y. Zhao, C. Shi, W. Zeng, B. Liao, M. Zhang and X. Tao, *RSC Adv.*, 2021, **11**, 25955–25960.

41 S. R. Patel, S. H. Chaki, R. K. Giri, A. J. Khimani, Y. H. Vaidya, P. Thakor, A. B. Thakkar and M. P. Deshpande, *ACS Appl. Bio Mater.*, 2023, **6**, 2211–2225.
42 Z. Zhou, W. Zhang, W. Zhao, Z. Yang and C. Zeng, *J. Electron. Mater.*, 2014, **43**, 359–368.
43 S. Yang, F. Ji, Z. Wang, Y. Zhu, K. Hu, Y. Ouyang, R. Wang, X. Ma and C. Cao, *Electrochim. Acta*, 2019, **324**, 134864.
44 Y. Zhang, Y. Zhu, Z. Wang, H. Peng, X. Yang, Y. Cao, C. Du, X. Ma and C. Cao, *Adv. Funct. Mater.*, 2021, **31**, 1–13.
45 Y. Li, D. Yan, Y. Zou, C. Xie, Y. Wang, Y. Zhang and S. Wang, *J. Mater. Chem. A*, 2017, **5**, 25494–25500.
46 Y. Z. Xu, C. Z. Yuan and X. P. Chen, *RSC Adv.*, 2016, **6**, 106832–106836.
47 E. Hao, H. Zhang, B. Yang, H. Ren and J. Shen, *J. Colloid Inter. Sci.*, 2001, **238**, 285–290.
48 Z. R. Parekh, S. H. Chaki, A. B. Hirpara, G. H. Patel, R. M. Kannaujiya, A. J. Khimani and M. P. Deshpande, *Phys. B*, 2021, **610**, 412950.
49 S. H. Chaki and A. Agarwal, *J. Cryst. Growth*, 2007, **308**, 176–179.
50 R. B. Shafizade, I. V. Ivanova and M. M. Kazinets, *Thin Solid Films*, 1978, **55**, 211–220.
51 E. M. Gavrushchuk, *Inorg. Mater.*, 2003, **39**, 883–899.
52 K. Breunig, I. Spahn, S. Spellerberg and H. H. Coenen, *Radiochim. Acta*, 2015, **103**, 397–402.
53 R. K. Giri, S. H. Chaki, A. J. Khimani, S. R. Patel and M. P. Deshpande, *Eur. Phys. J. Plus*, 2021, **136**, 320.
54 Z. S. Kachhia, S. H. Chaki, R. K. Giri, Z. R. Parekh, R. M. Kannaujiya, A. B. Hirpara, M. P. Deshpande and J. P. Tailor, *Mater. Today Proc.*, 2022, DOI: **10.1016/j.matpr.2023.02.240**.
55 R. M. Kannaujiya, A. J. Khimani, S. H. Chaki, S. M. Chauhan, A. B. Hirpara and M. P. Deshpande, *Eur. Phys. J. Plus*, 2020, **135**, 1–12.
56 P. Parthasarathy, M. Alherbawi, S. Pradhan, T. Al-Ansari, H. R. Mackey and G. McKay, *Biomass Convers. Biorefin*, 2022, DOI: **10.1007/s13399-021-02249-4**.
57 A. Nyombi, M. Williams and R. Wessling, *Energy Sources, Part A Recover. Util. Environ. Eff.*, 2018, **40**, 2660–2670.
58 P. Giannozzi, S. Baroni, N. Bonini, M. Calandra, R. Car, C. Cavazzoni, D. Ceresoli, G. L. Chiarotti, M. Cococcioni, I. Dabo, A. Dal Corso, S. De Gironcoli, S. Fabris, G. Fratesi, R. Gebauer, U. Gerstmann, C. Gougoussis, A. Kokalj, M. Lazzeri, L. Martin-Samos, N. Marzari, F. Mauri, R. Mazzarello, S. Paolini, A. Pasquarello, L. Paulatto, C. Sbraccia, S. Scandolo, G. Sclauzero, A. P. Seitsonen, A. Smogunov, P. Umari and R. M. Wentzcovitch, *J. Phys.: Condens. Matter*, 2009, **21**, 395502.
59 J. P. Perdew, K. Burke and M. Ernzerhof, *Phys. Rev. Lett.*, 1996, **77**, 3865.
60 M. B. Solanki, J. H. Joshi, P. M. Vyas, M. J. Joshi and B. B. Parekh, *Invertis J. Sci. Technol.*, 2017, **10**, 98.
61 W. S. Morgan, J. J. Jorgensen, B. C. Hess and G. L. W. Hart, *Comput. Mater. Sci.*, 2018, **153**, 424–430.
62 M. B. Solanki, S. Shinde and B. B. Parekh, *Mater. Today Proc.*, 2022, **67**, 943–947.
63 S. Patel, S. H. Chaki and P. C. Vinodkumar, *J. Appl. Phys.*, 2018, **124**, 215103.
64 J. P. Tailor, S. H. Chaki and M. P. Deshpande, *Nano Express*, 2021, **2**, 010011.
65 G. K. Solanki, D. N. Gujarathi, M. F. Deshpande, D. Lakshminarayana and M. K. Agarwal, *Cryst. Res. Technol.*, 2008, **43**, 179–185.
66 P. Peng, Z. N. Gong, F. S. Liu, M. J. Huang, W. Q. Ao, Y. Li and J. Q. Li, *Intermetallics*, 2016, **75**, 72–78.
67 A. Ducka, B. Trawiński, B. Bochentyn, A. Dubiel and B. Kusz, *Mater. Res. Bull.*, 2021, **133**, 111042.
68 Z. R. Parekh, M. P. Deshpande, S. V. Bhatt, H. R. Bhoi, R. M. Kannaujiya, Y. V. Joshi, S. J. Pandya and S. H. Chaki, *J. Alloys Compd.*, 2023, **968**, 171738.
69 D. Zhang, J. Yang, Q. Jiang, L. Fu, Y. Xiao, Y. Luo and Z. Zhou, *Artic. J. Mater. Chem. A*, 2016, **4**, 4188–4193.
70 B. Gahtori, S. Bathula, K. Tyagi, M. Jayasimhadri, A. K. Srivastava, S. Singh, R. C. Budhani and A. Dhar, *Nano Energy*, 2015, **13**, 36–46.
71 L. Yang, Z. G. Chen, G. Han, M. Hong, L. Huang and J. Zou, *J. Mater. Chem. A*, 2016, **4**, 9213–9219.
72 L. Yang, Z. G. Chen, G. Han, M. Hong and J. Zou, *Acta Mater.*, 2016, **113**, 140–146.
73 B. Q. Zhang, Y. Liu, Y. Zuo, J. S. Chen, J. M. Song, H. L. Niu and C. J. Mao, *Nanomaterials*, 2018, **8**, 8.
74 Y. Jin, M. K. Han and S. J. Kim, *Appl. Sci.*, 2017, **8**, 1–10.